



**HAL**  
open science

# Phosphonic Acid Fluorescent Organic Nanoparticles for High-Contrast and Selective Staining of Gram-Positive Bacteria

Joanna Boucard, Rym Boudjemaa, Karine K. Steenkeste, Cedric Jacqueline, Nicolas Stephant, François-Xavier Lefèvre, Adèle Laurent, Lenaïc Lartigue, Philippe Hulin, Steven Nedellec, et al.

## ► To cite this version:

Joanna Boucard, Rym Boudjemaa, Karine K. Steenkeste, Cedric Jacqueline, Nicolas Stephant, et al.. Phosphonic Acid Fluorescent Organic Nanoparticles for High-Contrast and Selective Staining of Gram-Positive Bacteria. *ACS Omega*, 2018, 3 (12), pp.17392-17402. 10.1021/acsomega.8b02603 . hal-02001014

**HAL Id: hal-02001014**

**<https://hal.science/hal-02001014>**

Submitted on 12 Nov 2022

**HAL** is a multi-disciplinary open access archive for the deposit and dissemination of scientific research documents, whether they are published or not. The documents may come from teaching and research institutions in France or abroad, or from public or private research centers.

L'archive ouverte pluridisciplinaire **HAL**, est destinée au dépôt et à la diffusion de documents scientifiques de niveau recherche, publiés ou non, émanant des établissements d'enseignement et de recherche français ou étrangers, des laboratoires publics ou privés.

# Phosphonic Acid Fluorescent Organic Nanoparticles for High-Contrast and Selective Staining of Gram-Positive Bacteria

Joanna Boucard,<sup>†</sup> Rym Boudjemaa,<sup>‡</sup> Karine Steenkeste,<sup>‡</sup> Cédric Jacqueline,<sup>‡</sup> Nicolas Stephant,<sup>§</sup> François-Xavier Lefèvre,<sup>†</sup> Adèle D. Laurent,<sup>†</sup> Lénaïc Lartigue,<sup>†</sup> Philippe Hulin,<sup>#</sup> Steven Nedellec,<sup>#</sup> Marie-Pierre Fontaine-Aupart,<sup>‡</sup> and Eléna Ishow<sup>\*,†,§</sup>

<sup>†</sup>CEISAM–UMR CNRS 6230, Université de Nantes, 2 rue de la Houssinière, Nantes 44322, France

<sup>‡</sup>ISMO UMR CNRS 8214, Université Paris-Saclay, Orsay 91405, France

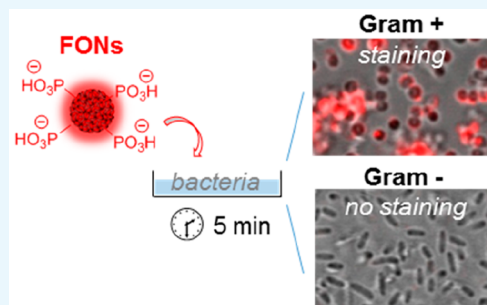
<sup>‡</sup>EA 3826 Thérapeutiques anti-infectieuses, Université de Nantes, IRS2 Nantes Biotech, 22 Boulevard Benoni Goullin, Nantes 44200, France

<sup>§</sup>IMN–UMR CNRS 6502, Université de Nantes, Nantes 44322, France

<sup>#</sup>INSERM UMS 016-UMS CNRS 3556, 8 quai Moncoussu, Nantes 44007, France

## Supporting Information

**ABSTRACT:** Fast and selective detection of pathogens represents high challenges given the considerably high proliferation rate and mutation potential of bacteria against antibiotics. With this aim, anionic red-orange-emitting fluorescent organic nanoparticles (FONs), characterized by high brightness and photostability, are developed to selectively stain *Staphylococcus aureus* after only 5 min of exposure. No cytotoxicity effects are observed as a result of the negatively charge surface of the employed FONs. By contrast, no staining can be observed with *Pseudomonas aeruginosa* strains. The exclusive labeling of Gram-positive bacteria is ascribed to originate from the phosphonic acid moieties incorporated in the FON-constituting fluorophores because model FONs, devoid of phosphonic acids, show no adhesion under the same experimental conditions. Tight hydrogen bonding between the FON acidic units and the peptidoglycan (PG) layers comprising the outer wall of *S. aureus* is suspected to be the prevailing factor for the encountered selective interactions. PG layers from *S. aureus* are employed to apprehend the interactions developed between FONs and the bacteria membrane. Correlative light electron microscopy using confocal fluorescence microscopy and SEM reveal FONs mainly located at extensively reorganized or “dented” PG areas. Such privileged localizations tend to suggest multivalent physicochemical interactions to aggregate a multifold of nanoparticles. Finally, spectral follow-up of the FON-stained bacteria membrane shows significant hypsochromic shift of the fluorescence emission, signaling progressive disassembly of FONs and a change of the surrounding polarity. This feature offers promising perspectives to use doped FONs as theranostic agents to liberate encapsulated antibiotics upon FON disintegration inside the bacteria membrane.



## 1. INTRODUCTION

Fast and selective detection of pathogens represents high technological and scientific challenges in the context of outbreaks or infections contracted after hospitalization to avoid dissemination and severe health complications. Stimuli-responsive nanostructured surfaces and nanoparticles have thus emerged to gain speed and portability.<sup>1–3</sup> Even though electrochemical biosensors,<sup>4</sup> as well as magnetic trapping and imaging of bacteria,<sup>5–7</sup> have revealed to be efficient, optical detection stirs particular attention because high-resolution and time-resolved mapping of bacteria surface can be achieved, giving access for instance to dynamic interactions with antibiotics.<sup>8</sup> It also enables higher levels of sensitivity, down to the zeptomolar concentration and single bacterium level.<sup>9</sup> This is particularly true when using bioconjugated gold nanoparticles, which yield neat red-to-blue colorimetric contrast due to bacteria recognition causing aggregation<sup>10</sup> or

provide sensitive vibrational fingerprint by resorting to surface-enhanced resonance spectroscopy.<sup>11,12</sup> Such level of sensitivity can also be achieved by using luminescent probes, especially fluorescent ones, implying highly sensitive detectors<sup>13</sup> and allowing for multiplexed detection.<sup>5</sup> The most classical approach involves bioconjugated pairs of plasmonic nanoparticles and luminophores, whose emission signal is switched on or off because of the close vicinity of the nanoparticles mediated by tight interactions with bacteria or the genetic material of bacteria, offering for instance micromolar to nanomolar detection of *Staphylococcus aureus*.<sup>14,15</sup> Another advantageous and simpler strategy relies on the use of intrinsically bright semiconductive polymers, functionalized

Received: September 30, 2018

Accepted: November 30, 2018

Published: December 14, 2018

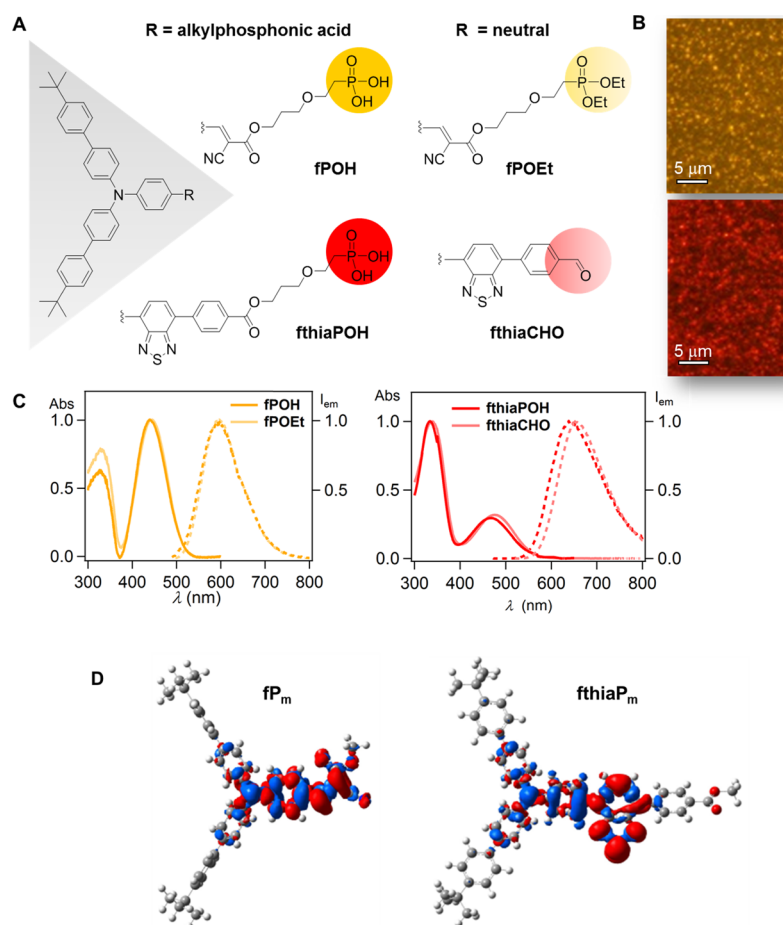


**Figure 1.** (A) Molecular phosphonic acid and model fluorophores constituting **fPOH**, **fPOEt**, **ftbiaPOH**, and **ftbiaCHO** FONs used in this study. (B) Wide-field fluorescence microscopy of a droplet of aqueous **fPOEt** and **ftbiaCHO** FON suspensions, after water evaporation ( $\lambda_{\text{exc}} = 480$  nm,  $\lambda_{\text{em}} > 520$  nm; objective 60 $\times$ , NA = 1.43, true colors recorded with a color camera). Scale bar: 10  $\mu\text{m}$ . (C) Normalized absorption (bold line) and emission (dashed line) spectra of phosphonic acid and model FONs in Millipore water ( $\lambda_{\text{exc}} = 465$  nm). (D) Electronic density difference between the excited and ground states for computed model fluorophores **fp<sub>m</sub>** and **ftbiaP<sub>m</sub>**, where the alkoxy chain has been replaced with a methyl group. The red (blue) zones indicate increase (decrease) in the electronic density upon electronic transition.

with cationic or sugar units to target the bacteria wall, as demonstrated by a seminal work showing the detection of less than  $10^4$  *Escherichia coli* units.<sup>16</sup> Such approach was recently completed with the fabrication of fluorescent organic nanoparticles (FONs), issued from the self-assembly of positively charged polymers with complementary negatively charged linkers<sup>17</sup> or small cationic and amphiphilic fluorophores.<sup>18,19</sup> When compared to semiconjugated polymers, small fluorophore-based FONs offer larger structural control and versatility, as well as less emission sensitivity, on conformational changes of the  $\pi$ -conjugated backbone. Moreover, because they are exclusively composed of  $10^4$  to  $10^5$  fluorophores, higher contrast and less photobleaching than those encountered with individual fluorophores can be achieved. For all the abovementioned structures, specific chemical units have thus been introduced to promote tight interactions with the bacteria surface, whose external composition classifies bacteria into Gram-positive and Gram-negative strains.<sup>20</sup> The outer wall of Gram-positive bacteria contains peptidoglycans (PGs) as major constituents that consist of a 15–100 nm thick multilayer of linear glycan strands based on the repetition of disaccharide units (more precisely *N*-acetylglucosamine and *N*-acetylmuramic acid) and cross-linked with short peptide chains.<sup>21</sup> This basic structure,

undergoing a large chemical or architectural variety, forms a continuous envelop, ensuring among others the rigidity of the underneath cytoplasmic phospholipid membrane to withstand cell turgor pressure.<sup>22</sup> This alternating network is completed by teichoic acid, a wall-transversing linear polymer of phosphodiester-linked glycerol phosphate, covalently bound to phospholipids, aiming at regulating enzymes responsible for the membrane autolysis and participating in cell adhesion, development, and signaling.<sup>23</sup> On the other hand, the cell membrane of Gram-negative bacteria is composed of a lipopolysaccharide outer leaflet and an inner cytoplasmic membrane sandwiching a thin (5–10 nm) layer of PGs, devoid of teichoic acid. Given the oligosaccharide composition of the bacterial cell walls, numerous effort has been accomplished in the fabrication of carbohydrate-functionalized nanomaterials for the mutual interplay with bacteria.<sup>24</sup> However, strains display differentiated interactions regarding the family of carbohydrates (mannose, galactose, rhamnose, ...),<sup>16</sup> limiting the ubiquity of the functionalization strategy.<sup>25</sup> Another approach implies the introduction of positively charged nanomaterials by resorting to small cationic ligands or polyelectrolytes made of ammonium, pyridinium, or pyrimidinium moieties, which can interact with the phosphate or carboxylate units that impart bacteria with a negative surface

potential.<sup>17,26,27</sup> Such tight electrostatic binding nevertheless systematically revealed to be deleterious because of strong membrane polarization change, causing neat flow of ions and severe membrane lysis.<sup>26,28</sup> Yet, toxicity effects, highly sought for the design of antibiotics, represent a severe issue for long-term observation.<sup>29</sup> Contrary to the first expectations, nanomaterials with a negatively charged surface have also shown extensive adsorption on the bacteria membranes; they have thus very recently appeared as an attractive alternative given their relative innocuity.<sup>30</sup> Carboxylate units represent the most commonly investigated anionic ligands for such nanomaterials and are reported to establish strong hydrogen bonds with the complementary hydroxyl groups of the glycosylated polymers or the amino acid units of the peptide chains of the bacterial outer membrane.<sup>30,31</sup> Curiously, alkylphosphonic acid units have only been scarcely investigated as potential promoters of nanoparticle–bacteria adhesion, despite their multivalent hydrogen bonding ability with H-donating units and their one- and twofold deprotonated states, characterized by acido-basicity constants  $pK_{a1} = 1.1–2.3$  and  $pK_{a2} = 5.7–8.2$ , respectively, in the presence of electron-withdrawing or -donating substituents.<sup>32,33</sup> Yet, the positive impact of phosphonic acid containing hydrogels on cell growth and proliferation has already been reported for eukaryotic cells, such as fibroblasts and osteoblasts, involved in bone repairing, due to efficient swelling in water and protein binding.<sup>34</sup> Such studies echoed with similar microbial observations when octadecylphosphonic acid, acting as an amphiphilic constituent of multilayered Langmuir–Blodgett films, revealed to be less efficient than its analogous hydroxamic acid to inactivate biofilm formation on glass surfaces when exposed to *Acidithiobacillus ferrooxidans* bacteria, causing severe biocorrosion.<sup>35</sup> Even more striking is the occurrence of natural phosphonic acids in living organisms,<sup>36,37</sup> especially (1*R*,2*S*)-epoxypropylphosphonic acid, dubbed as fosfomycin,<sup>38</sup> which was isolated from Gram-positive *Streptomyces* strains (*S. fradiae*, *S. wedmorensis*, and *S. viridochromogenes*).<sup>39</sup> This compound, nowadays broadly used as an antibiotic against *S. aureus*, cystitis, and gastrointestinal infections, among others, was shown to inhibit enzymes involved in the biosynthesis of bacterial cell wall.

To overcome the current shortcomings in terms of phosphonic acid coatings of fluorescent nanomaterials and contact investigations with bacteria, we have devised FONs made out of small  $\pi$ -conjugated fluorophores incorporated with phosphonic acid moieties. Two bacteria strains, *S. aureus* and *Pseudomonas aeruginosa*, Gram-positive and Gram-negative bacteria, respectively, have been investigated as they are responsible for more than 25% of the nosocomial bacterial infections contracted in hospitals after invasive monitoring or surgery. Therefore, fast detection is a major preoccupation to which FONs, mainly employed for a decade to image eukaryotic cells<sup>40,41</sup> or more recently to transport anticancer drugs,<sup>42</sup> are expected to respond with efficacy. FON architecture is indeed akin to that of nanoparticles functionalized with small ligands or polyelectrolytes, which have been reported to develop tighter interactions with the bacterial outer membrane than those exerted by free charged polymeric chains, displaying an apparent lesser charge density.<sup>26</sup> Because FONs are intrinsically fluorescent, live cell imaging using optical microscopy could be performed without requiring additional staining of the bacteria membrane, subject to rearrangement in the presence of supplementary interacting

entities.<sup>43</sup> Complementary investigations with model nanomaterials devoid of phosphonic acid and correlative optical and electron microscopy imaging of PGs, major constituents of the bacterial cell outer wall, have also been performed to assess the efficacy and selectivity in the nanoparticle attachment onto bacteria.

## 2. RESULTS AND DISCUSSION

**2.1. Design of the FONs.** Two series of phosphonic acid derivatives **fPOH**<sup>44</sup> and **fthiaPOH**,<sup>42</sup> previously employed to investigate breast and adenocarcinoma cancer cells, were retained (Figure 1A).

In each series, any potential artifact related to distinct  $\pi$ -conjugation and the hydrophobic interactions thereof could be ruled out because the corresponding model and phosphonic acid compounds solely differ by their terminal units. Both **fPOH** and **fthiaPOH** phosphonic acids were obtained after deprotecting the phosphonate ester derivative **fPOEt** by using tris(trimethylsilyl)bromide or reacting an ethylenoxybromide precursor **fthiaBr** with tris(trimethylsilyl)phosphite following an Arbuzov mechanism, respectively. **fPOEt** was thus chosen as a model compound for **fPOH**, whereas the aldehyde precursor **fthiaCHO** was selected instead of **fthiaBr** as a model compound for **fthiaPOH**. Because the aldehyde unit is more polar than a bromine atom, **fthiaCHO** displayed more similarities to the **fPOEt** phosphonate counterpart in terms of van der Waals interactions. The requirements for FON formation in water and emission in the solid state were assured by the sterically crowded hydrophobic triaryl amino extremities.

In this way, FONs were simply obtained upon self-assembling the abovementioned small hydrophobic fluorophores after precipitating into a large amount of water a small aliquot of a concentrated dye solution, prepared in THF, a water-miscible solvent.<sup>45</sup> Well-dispersed nanospheres were obtained as revealed by TEM imaging (Figure 2), which showed no aggregation or flocculation over time.

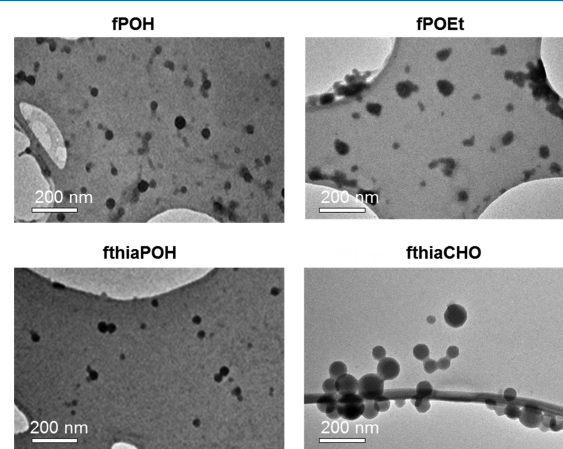


**Figure 2.** TEM imaging of FON dispersions deposited on holey carbon coated copper grids.

Their mean diameters  $d_{\text{TEM}}$  were measured by TEM, providing nanoparticle images with much lower contrast than that usually observed for inorganic nanoparticles given the exclusive presence of light elements. Manual counting of more than 300 nanoparticles was then performed and results in quite a narrow size polydispersity  $\sigma$ , less than 0.20.  $d_{\text{TEM}}$  values were found to be around 25 nm for phosphonic acid FONs,

significantly smaller than those for FON models. This difference in size stems from the more hydrophobic character of the compounds devoid of phosphonic acids and self-assembling into larger nanoparticles issued from a nucleation–aggregation growth process.<sup>46</sup> The surface  $\zeta$ -potential was found to be largely negative by zetametry, ensuring large colloidal stability with respect to the FON size (Table 1). The

**Table 1. Structural (TEM and DLS Analyses) and Photophysical Characteristics of FONs**

FON	$d_{\text{TEM}}^a$ ( $\sigma$ ) <sup>a</sup> (nm)	$\zeta$ (mV)	$\lambda_{\text{max}}^{\text{(abs)}}$ (nm)	$\lambda_{\text{max}}^{\text{(em)}}$ (nm)	$\Phi_f^b$
fPOH	28 (0.17)	$-33 \pm 3$	440, 326	605	0.01
fPOEt	83 (0.11)	$-36 \pm 4$	443, 329	613	0.05
fthiaPOH	24 (0.20)	$-26 \pm 1$	466, 335	645	0.02
fthiaCHO	65 (0.12)	$-24 \pm 5$	476, 339	654	0.27

<sup>a</sup>From lognormal distribution. <sup>b</sup>Measured from coumarin 540 A in EtOH. Steady-state fluorescence measurements were performed in Millipore water.

intriguing similar  $\zeta$ -values for the phosphonic acid and model FONs can be attributed to strong polarization of water molecules surrounding the dipolar dyes,<sup>47</sup> although their clear origins are still widely unknown.

**2.2. Interpretation of the FON Photophysical Properties.** Both phosphonic acid and model FONs display an absorption band in the blue [ $\lambda_{\text{max}}^{\text{(abs)}} = 440\text{--}476$  nm], while emitting in the orange-red [ $\lambda_{\text{max}}^{\text{(em)}} = 594\text{--}654$  nm] region of the visible spectrum (Figure 1B,C). It is worth noting that no significant light scattering by FONs took place as exemplified by the flat baseline above 550 nm, as a result of the light element content of FONs when compared to inorganic nanoparticles with similar sizes. Such feature allowed us to resort to classical photophysical measurements in homogeneous solutions without requiring the use of integrating sphere, neither in absorption nor in emission. The large Stokes shift of up to  $5900\text{ cm}^{-1}$  that could be noticed for all FONs originates from the strong charge transfer undergone in the excited state from the electron-donating amino group to the electron-withdrawing group, namely, the cyanovinylidene or benzothiadiazole moiety. To gain computation time, the alkoxyphosphonic acid terminal chains for fPOH and fthiaPOH could be replaced with a methyl group because they are not conjugated with the rest of the molecule (Figure S1). To apprehend the spatial extension of the charge transfer, vertical excitation energies of the model compounds fP<sub>m</sub> and fthiaP<sub>m</sub> were computed using TDDFT. Computed electronic density difference between the first excited state and the ground state of the corresponding compounds clearly depicts a charge transfer with a loss of density (blue zone in Figure 1D) on the central amino group and a gain of electronic density on the cyano or benzothiadiazole group (red zone in Figure 1D). Such computations thus show the intrinsically stronger push–pull character for fthiaY compounds, with both a larger amount and distance of the charge transfer between the states (see Supporting Information for more computational details – Table S1 and Figure S2). As for the emission properties, it is worth noting that fthiaY (Y = CHO, POH) derivatives show a significantly red-shifted fluorescence band, peaking at 645–654 against 605–613 nm for the fX (X = POEt, POH) compounds, owing to the benzothiadiazole unit increasing the  $\pi$ -conjugated pathway (4.37 and 4.53 vs 3.24 Å)

and the electron-deficient part within the push–pull structure (Table S1). A last noteworthy feature relates to the fluorescence quantum yields  $\Phi_f$  for fthiaY compounds ( $\Phi_f = 2\text{--}27\%$ ) that are significantly higher than those for fX ( $\Phi_f = 1\text{--}5\%$ ) (Table 1). Such discrepancy stems from the more flexible structure for fX compounds, where rotation of the bridging phenyl ring contributes to the relaxation of the Franck–Condon excited state in a radiation-less manner as earlier established by ultrafast transient absorption spectroscopy.<sup>48</sup> The additional observation of reduced brightness for the phosphonic acid derivatives compared to that of their model counterparts has also been interpreted as a consequence of intermolecular hydrogen bonds between the phosphonic acid themselves inside the nanoparticles and/or with the surroundings. Partial quenching through vibrational coupling with the O–H oscillators emanating from  $-\text{PO}_3\text{H}$  units (and their deprotonated forms) and water molecules had indeed been established by time-resolved fluorescence measurements, thereby demonstrating the great capacity of the acidic units to generate extensive hydrogen bonding.<sup>42</sup>

**2.3. Selective Interactions with Gram-Positive Bacteria.** To test the ability of FONs to interact with bacteria, we first focused on Gram-positive *S. aureus* strains, harvested in their stationary phase and incubated with FONs for 5 min. After FON excess removal, fluorescence confocal laser scanning microscopy of the bacterial suspensions pointed out systematic spatial correspondence between fthiaPOH or fPOH FONs and *S. aureus* as established from the overlapping fluorescence and transmission imaging ( $\lambda_{\text{exc}} = 488$  nm,  $\lambda_{\text{em}} = 520\text{--}580$  nm) (Figure 3). No such matching occurred for the model fthiaCHO and fPOEt FONs forming bright aggregates next to the bacteria (Figure 3).

To identify the local distribution of FONs, namely, at the surface or inside *S. aureus*, the samples were stained with SYTO 61, a marker lighting up in the near-infrared upon binding with DNA and compatible with live cell imaging conditions. Because the absorption spectra of FONs [ $\lambda_{\text{max}}^{\text{(abs)}} = 440\text{--}460$  nm] and SYTO 61 [ $\lambda_{\text{max}}^{\text{(abs)}} = 618$  nm] did not overlap, differentiated excitation wavelengths could be used for independent visualization of FONs and SYTO 61 (Figure S3). For the sake of clarity, false green color was attributed to SYTO 61 and red color was attributed to FONs. Z-stack acquisitions and recombination for both excitation wavelengths systematically showed for stained *S. aureus* fine red lines surrounding a large central green area, with no co-localization between the emitting dyes. These clear patterns let us reasonably conclude that fPOH and fthiaPOH phosphonic acid FONs tightly bind to the cell surface and do not penetrate into the cytoplasm, where SYTO 61 accumulates (Figure 4). At this stage, it is worth mentioning the remarkably high photostability of FONs over long periods of illumination (10–20 min) compared to that of the SYTO 61 molecular dye, undergoing fast fainting in the observation conditions herein adopted.

When extended to Gram-negative *P. aeruginosa* strains, confocal imaging revealed striking differences. No phosphonic FONs collocated with bacteria could be detected, and the few visible red spots originated from residuals FONs remaining after the washing step (Figure 5).

As expected from the above results, staining *P. aeruginosa* with fPOEt was again found ineffective (Figure S4). Because FONs remain at the periphery of *S. aureus* and do not undergo cell uptake, size effects to explain the differentiated interactions

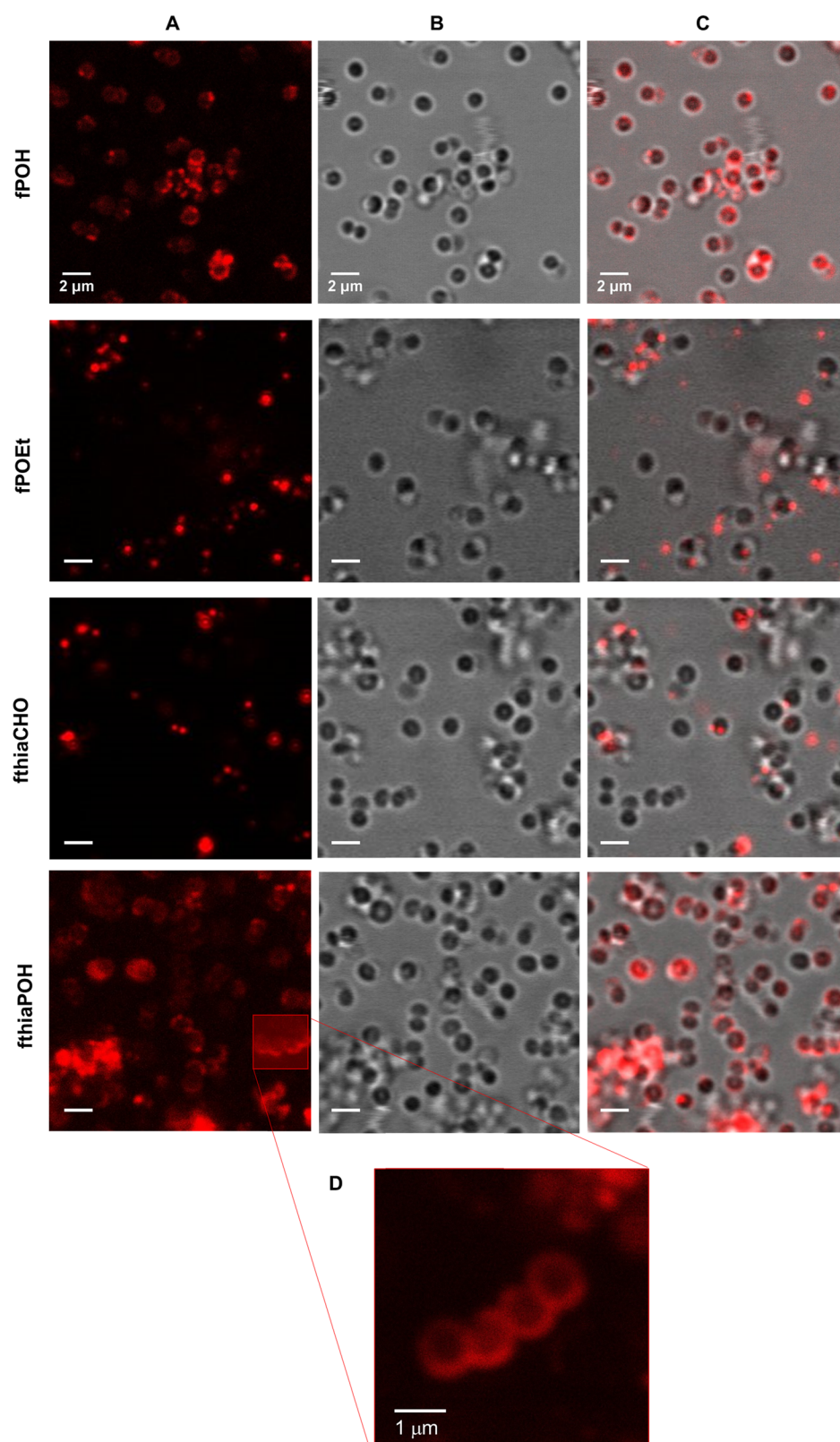


**Figure 3.** Confocal fluorescence microscopy imaging of *S. aureus* incubated with phosphonic acid **fPOH** and **fthiaPOH** FONs and **fPOEt** and **fthiaCHO** model FONs in physiological water. (A) Fluorescence imaging, (B) transmission, (C) merged transmission and fluorescence imaging, (D) zoom-in of **fthiaPOH** FON fluorescence imaging ( $\lambda_{\text{exc}} = 488 \text{ nm}$ ,  $\lambda_{\text{em}} = 520\text{--}580 \text{ nm}$ ). Scale bar:  $2 \mu\text{m}$  when non-specified.

of phosphonic acid FONs, smaller than their neutral model counterparts, can reasonably be ruled out. Compared to eukaryotic cells involving either receptor-mediated endocytosis or large membrane deformation, such size effects are expected

to be negligible, especially because the outer wall of *S. aureus* strains displays elastic moduli  $G$  ( $G = 0.6\text{--}95 \text{ MPa}$ ),<sup>49</sup> one to three orders of magnitude higher than that of the most common mammalian cells.<sup>50</sup> The present results rather tend to

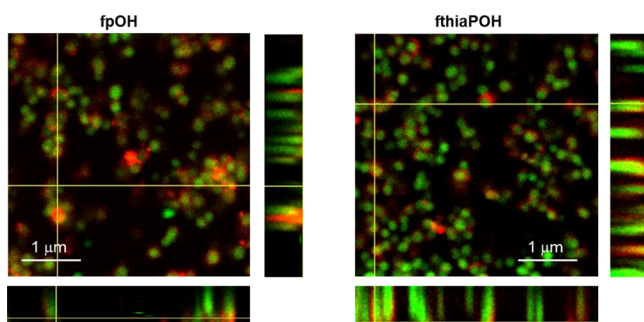


**Figure 4.** Confocal fluorescence microscopy imaging of *S. aureus* labeled with phosphonic **fPOH** or **fthiaPOH** FONS ( $\lambda_{\text{exc}} = 488$  nm,  $\lambda_{\text{em}} = 520$ –580 nm) and stained with SYTO 61, a nucleic acid marker ( $\lambda_{\text{exc}} = 633$  nm,  $\lambda_{\text{em}} = 650$ –750 nm). The images result from merging acquisitions obtained after separate excitation at 488 and 633 nm. Right and bottom strips:  $x$ - and  $y$ -projections. Red and green colors correspond to FONS and SYTO 61 emission, respectively.

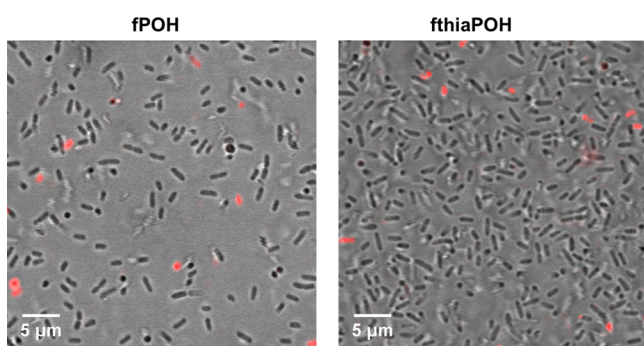


**Figure 5.** Merged transmission and fluorescence imaging from laser scanning confocal microscopy of *P. aeruginosa* incubated with phosphonic acid **fPOH** and **fthiaPOH** FONS ( $\lambda_{\text{exc}} = 488$  nm,  $\lambda_{\text{em}} = 520$ –750 nm).

illustrate the privileged role played by phosphonic acid moieties to strongly and specifically bind the outer surface of Gram-positive bacteria such as *S. aureus*. We here suspect prominent interactions through hydrogen bonds mediated by the strong hydrogen-donating and -accepting character of the phosphonic acidic units. This assumption is based on previous studies reporting the importance of hydrogen bonding exerted by vancomycin- or daptomycin-functionalized nanoparticles as the prevailing driving force for adhering on the peptido-layer of Gram-positive bacteria.<sup>51,52</sup>

**2.4. Spectral Observations of FON Disassembling.** To test the long-term effects of phosphonic FONS interacting with bacteria, we looked at the emission signal coming from the bacteria membrane after 24 h. Spectral follow-up by confocal

fluorescence microscopy showed a clear hypsochromic 30 nm shift of the emission maximum, suggesting either significant reorganization of the cell surface or FON structural change (Figure 6).

We first assessed the absence of significant toxicity caused by FONS by recording time-kill curves. No impact of the FON presence was observed on both the kinetics of bacterial growth and bacterial counts after 3, 6, and 24 h (Figure S5). As for assessing possible cell membrane damage, we used propidium iodide (PI), a red-emitting intercalating agent that can only penetrate compromised membrane cells. Viability observation using fluorescence microscopy ( $\lambda_{\text{exc}} = 543$  nm,  $\lambda_{\text{em}} = 640$ –750 nm for PI;  $\lambda_{\text{exc}} = 488$  nm,  $\lambda_{\text{em}} = 520$ –780 nm for FONS) of both control (non-FON-treated) and FON-treated bacterial strains showed the same extent of membrane damage (Figure S6). These results thus confirm the innocuity of negatively charged nanoparticles over positively ones, in contrast to a recent work on cationic FONS incorporating fluorescent pyridinium entities.<sup>18</sup> They tend to suggest that the measured spectral shift may rather be related to FON evolution. Nevertheless, spectral follow-up over 24 h of aqueous FON dispersions in the absence of *S. aureus* showed no significant evolution, neither in energy nor in intensity (Figure S7). As **fPOH** and **fthiaPOH** exhibit strong solvatochromism from orange red in a polar solvent (e.g., THF) and as FONS to green yellow in hydrocarbon solvents, such as toluene (Figure S8, Table S1), we would rather suspect the participation of hydrophobic biological units of the cell membrane, amenable to progressively dissolve FONS and solvate the resulting individual fluorophores. Such assumption is based on previous studies dedicated to the temporal evolution of orange-emitting FONS comprising similar small solvatochromic fluorophores and exposed to eukaryotic cells, such as macrophages<sup>53</sup> or cancer cells.<sup>42</sup> After FON incubation and cellular uptake, the expulsion of bright-green vesicles in the case of macrophages or the formation of an intense and continuous green halo in the cytoplasm of cancer cells was interpreted as a result of extensive FON disassembly by the lipid content of the vesicle membranes or endosomal compartments. When looking at the composition of the cell wall, lipoteichoic acid (LPA), one of the two major constituents, could indeed come into play as its repetitive glycolipid units impart LPA with strong hydrophobic interactions. We thus suspect hydrophobic solvation by the surrounding LPA chains, mediated by FON attachment through tight hydrogen bonds to the PG layers of the outer wall, to be involved in the observed spectral shift.

**2.5. PG Layers To Apprehend the Interactions between FONS and *S. aureus*.** Because Gram-positive bacteria differ from Gram-negative ones through the presence

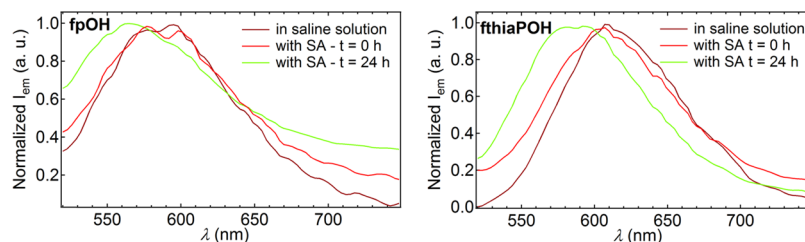


**Figure 6.** Spectral evolution of the emission spectrum of *S. aureus* bacteria incubated with **fPOH** (left) and **fthiaPOH** (right) FONS after 0 h (actually, 5 min after incubation) and 24 h ( $\lambda_{\text{exc}} = 480$  nm,  $\lambda_{\text{em}} > 520$  nm). The reference spectrum of FONS in sterile saline water ( $9 \text{ g L}^{-1}$ ) is depicted in brown.

of multilayered PGs mainly constituting their outer cell wall, we retained PGs issued from *S. aureus* to gain insight into the specific interactions encountered by the phosphonic acid FONs with the bacteria membrane. We resorted to commercial lyophilized extracts that were reconstituted in Millipore water at a  $0.15 \text{ mg L}^{-1}$  concentration and mixed with FON solutions. After smooth agitation for 5–10 min, the suspension was delicately centrifuged and rinsed twice to remove excess FON in the supernatant. Wide-field fluorescence microscopy imaging under 488 nm excitation unveiled large and green autofluorescent debris of PGs, extensively coated by phosphonic acid FONs **fPOH** and **ftiaPOH**, appearing as small bright yellow and orange-red spots, respectively (Figure 7). Conversely, no FON adhesion could be observed in the

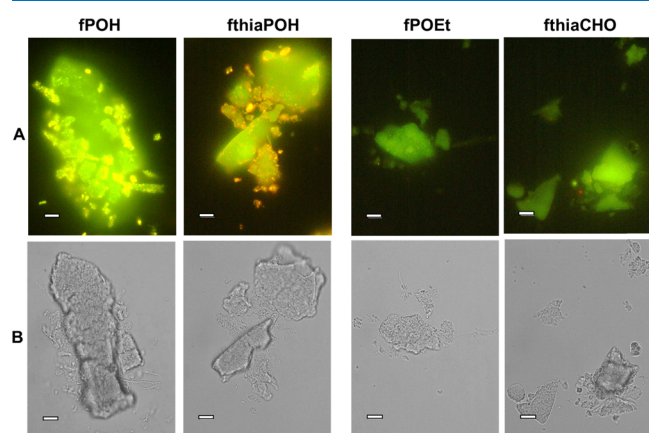


**Figure 7.** Wide-field fluorescence microscopy of PGs from *S. aureus* treated with phosphonic acid and model FONs: (A) fluorescence imaging ( $\lambda_{\text{exc}} = 480 \text{ nm}$ ,  $\lambda_{\text{em}} > 520 \text{ nm}$ , true colors, color camera), (B) transmission imaging. Scale bar:  $10 \mu\text{m}$ .

case of the model FONs **fPOEt** and **ftiaCHO** in the same lapse of time. The little distinguishable emissive spots correspond to the few FONs remaining after the washing steps and being fully mobile contrary to their phosphonic acid counterparts, firmly attached to PGs (Figure 7).

A quite intriguing feature relates to the global enhancement of the PG autofluorescence in the presence of **fPOH** and **ftiaPOH** and the notable discrepancy in terms of emission colors recorded using a color camera between FONs (Figure 1B) and FONs interacting with PGs (Figure 7). Steady-state fluorescence measurements of the suspensions revealed intractable analyses of the emission spectra because of the strong and broad signal from the PG suspension. By contrast, the first supernatant fraction after purification, containing little biological materials, displayed unexpectedly strong enhancement and noticeable hypsochromic shift of the emission signal for phosphonic FONs after mixing with PGs when compared to pristine FON solution. No such feature could be noticed with the FON models, keeping almost the same energy and intensity of their emission band, be they exposed or not to PGs (Figure S9). All these features recall the observations reported with *S. aureus* and thus showed that commercial PGs can serve as an easy and reliable model to assess the adhesion between FONs and the outer membrane of bacteria. We must admit that, at this step, we ignore the chemical or protein identity of the units interacting with FONs and conducting to their partial disassembling. Raman spectroscopy, beyond the scope of the

current studies, could present an attractive tool in the future to help us investigate the structure of the interacting entities.

To gain spatial resolution of PGs interacting with FONs, SEM and confocal fluorescence microscopy were performed on the samples in a correlative manner using TEM holey carbon coated finder grids. SEM imaging of the PG sacculi revealed relatively flattened envelopes compared to their original spherical shape for untreated *S. aureus* in their normal state (Figure S11). Damaged envelopes, appearing as craters or burst cells, could also be noticed and recalled previous SEM investigations of *S. aureus* treated with antibiotics.<sup>54</sup> Fine correlation between SEM and confocal fluorescence microscopy imaging revealed systematic co-localization of strongly emissive spots with PG “crushed” regions (Figure 8). It is

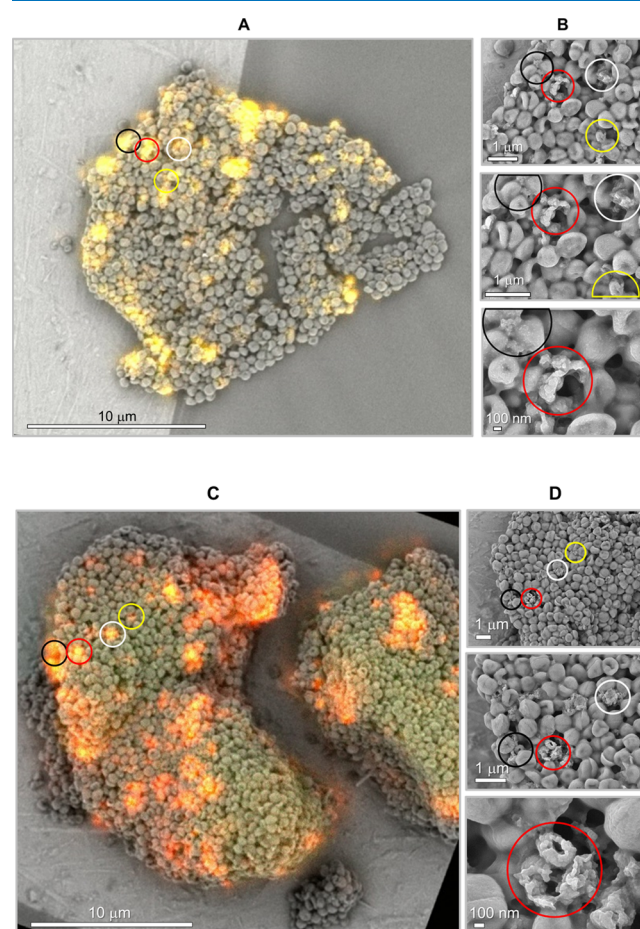


**Figure 8.** PG from *S. aureus* after treatment with **fPOH** (A,B) and **ftiaPOH** (C,D). (A–C) Correlative light electron microscopy using SEM (3 kV, 4.4 mm working distance) and confocal fluorescence imaging ( $\lambda_{\text{exc}} = 480 \text{ nm}$ ,  $\lambda_{\text{em}} > 520 \text{ nm}$ ). (B–D) Progressive magnification using SEM imaging. Correlated areas are indicated by colored circles.

important to mention here that all samples were deposited on the carbon side of the grids, which advantageously led to strong emission quenching of FONs placed underneath close to the carbon side, as exemplified by a 3D-imaging stack (Figure S10). Hence, FONs interacting at the upper PG layers mostly contribute to the emission signal recorded under confocal conditions and could correlate with SEM imaging, also probing the upper surface of PG layers. These features could clearly be found for both **ftiaPOH** and **fPOH** FONs

that accumulated on these regions as demonstrated by the corresponding colored circles indicated on the progressively magnified SEM images. FONs here cannot be distinguished from the “dented” areas given their similar dimensions and electronic contrast from those of the “dented” areas. (Figure S12). As phosphonic FONs have proved to be non-cytotoxic, we can unambiguously rule out their role in the formation of PG dented areas. Here also, damage caused by SEM observations in vacuum and water evaporation can be discarded because only a few of PG sacculi are impacted. So, we suspect that such dented areas preexist before deposition on the TEM grid given the quite large stiffness of the PG layers of *S. aureus* (vide supra) that are little subjected to deformation upon mild deposition on the grid. The unexpected and specific FON localization recalls the anisotropic aggregation reported for gold nanoparticles interacting with *Bacillus subtilis*, another Gram-positive bacteria,<sup>55</sup> and suggests heterogeneous microscopic organization of the wall constituent units that would promote privileged and multivalent physicochemical interactions to aggregate a multifold of nanoparticles. The large roughness of the dented areas suggests the occurrence of multiple interactions that operate only with phosphonic acid FONs. Therefore, future experiments combining atomic force microscopy with confocal Raman and fluorescence microscopy will present crucial approaches to correlate any spectral differences between the diversely interacting PG regions and help gain insight into the underlying microscopic factors and chemical origin of the interactions.

These observations, describing comparative nanoparticle adhesion between bacteria and PGs, have never been reported up to now and should therefore provide stimulating routes to explore the design of novel bacterial sensors without requiring the grafting of costly and fragile antibodies.<sup>56</sup>

### 3. CONCLUSIONS

For the first time, to our knowledge, FONs incorporating small fluorophores with phosphonic acid units have been harnessed to specifically label Gram-positive bacteria such as *S. aureus* with a high contrast in physiological water, without requiring any immunoconjugation. Labeling was operated at the cell surface of bacteria that was found to be highly photostable with no deleterious impact on bacterial growth. Such privileged interactions, absent in the case of Gram-negative strains, could be attributed to strong hydrogen bonding developed between the FON phosphonate moieties and the cross-linked PG layers of the cell outer wall. Correlative light electron microscopy using SEM and confocal fluorescence imaging revealed specific FON localizations on dented PG areas, letting us to assume strong interactions between FONs and the membrane. Additional hydrophobic interactions, established between the aromatic backbone of the fluorophores and the lipid content of the LPA chains, another major constituent of the outer wall, have been proposed to participate in the progressive disassembly of FON inside the wall over time. Such FON structural evolution opens the pathway to vectorization and potential diffusion through the membrane of antibiotics that could be incorporated in FONs during their fabrication process. Further investigations on other strains of bacteria and fungi will be carried out to extend the potential of the current phosphonic acid derived FONs for fast and selective bacterial recognition, especially in complex physiological media.

## 4. EXPERIMENTAL SECTION

### 4.1. FON Solution Fabrication and Characterizations.

**4.1.1. FON Dispersion Fabrication.** Stock solutions of fX ( $X = \text{POEt}, \text{POH}$ )<sup>45</sup> and fthiaY ( $Y = \text{CHO}, \text{POH}$ )<sup>42</sup> fluorophores were prepared in spectrophotometric grade THF, such that the molar concentrations were equal from one sample to another (here around  $1.45 \text{ mmol L}^{-1}$ ). A small amount of the stock solution ( $50 \mu\text{L}$ ) was injected in one shot under vigorous stirring into a larger volume of Millipore water ( $2.5 \text{ mL}$ ) by means of a vortex.

**4.1.2. FON Structural Characterizations.** TEM micrographs were carried out on a JEOL JEM 1230 operated at 80 kV. All FON solutions were deposited onto holey carbon coated copper grids (300 mesh, Oxford Instruments). The size distribution of FONs was determined through manual counting of a larger number of nano-objects (300–500) using Image J software. Mean diameters and standard deviations were obtained by fitting the histograms with a lognormal function. Measurements of surface  $\zeta$ -potential were carried out by means of a Zetasizer Nano ZS ZEN 3600 (Malvern). The samples were placed in disposable folded capillary cells (DTS1070). Four measurements were realized for each sample, and the  $\zeta$ -potential was calculated from electrophoretic mobility dispersion fitted by the Smoluchowski model.

**4.1.3. Photophysical Characterizations.** UV–visible absorption spectra were recorded using a Varian Model Cary SE spectrophotometer equipped with a DRA 2500 integrating sphere. Molar absorption coefficients were obtained by an average of at least two measurements with less than 10% variation. Fluorolog-3 spectrofluorometer was used (HORIBA Jobin Yvon). Correction for the emission spectra in regard to the spectral response of the detector was automatically applied. Fluorescence quantum yields were determined in solution, referred to as coumarin 540 A in EtOH ( $\Phi_f = 0.38$ ).

**4.2. PG Layer Suspensions.** PG from *S. aureus* (#77140) were purchased from Aldrich. They were obtained from a suspension of *S. aureus* that was washed with NaCl solution ( $0.14 \text{ mol L}^{-1}$ ), suspended in 10% trichloroacetic acid, and eventually centrifuged. The residue was treated with trypsin/Tris solution (pH 8.0), filtered, washed with water, dialyzed, and lyophilized. PG suspensions were prepared at a  $0.15 \text{ mg L}^{-1}$  concentration in Millipore water. FON–PG mixtures were fabricated by mixing the PG suspension ( $950 \mu\text{L}$ ) with FON dispersion ( $50 \mu\text{L}$ ). After 10 min incubation, the suspensions were smoothly centrifuged ( $5000g$ , 3 min). The supernatant was removed and replaced with Millipore water ( $1 \text{ mL}$ ). The centrifuge-rising operation was repeated once more to efficiently removed FONs in excess.

**4.3. Microbiology Experiments.**  
**4.3.1. Bacterial Strain and Growth Conditions.** The collection strains methicillin-susceptible *S. aureus* (ATCC 27217) and *P. aeruginosa* PA01 were cultured in Tryptic Soy Broth (TSB) for growth overnight at  $37 \text{ }^\circ\text{C}$ . Bacterial counting was performed on agar plates and expressed as a number of colony forming units (cfu), which corresponds to  $10^6$  in the adopted culture conditions. The bacteria were then harvested in their stationary phase and washed twice by centrifugation using sterile saline solution ( $150 \text{ mmol L}^{-1} \text{ NaCl}$ ). The bacteria were then resuspended in TSB or saline solution ( $950 \mu\text{L}$ ).

**4.3.2. FON Incubation with Bacteria.** FON dispersions ( $50 \mu\text{L}$ ) were added to the bacterial strains resuspended in saline

water ( $9 \text{ g L}^{-1}$  NaCl), which corresponds to a FON:bacterium ratio of around  $10^4$ . After incubation at  $37^\circ\text{C}$  for 10 min, the mixtures were centrifuged ( $7000g$ , 5 min) and rinsed twice using saline water. The final cell pellet was resuspended in 1 mL of saline water. Aliquots of each preparation were directly placed in the wells of a Lab-Tek chamber slide for live observation using fluorescence confocal laser scanning microscopy. For samples spectrally investigated after 24 h, the previously described harvesting and rinsing protocol was applied only one day after.

**4.3.3. Bacteria staining with nucleic acid and viability markers.** Bacteria were treated with  $2.5 \mu\text{M}$  SYTO 61 (Invitrogen), a cell-permeant near-infrared fluorescent nucleic acid stain, to assess FON localization or PI (Invitrogen;  $5 \mu\text{L}$  from a  $1 \text{ mg mL}^{-1}$  solution), a red-emitting DNA intercalating marker that can only penetrate damaged-membrane cells, to assess strain viability upon interaction with FONs. SYTO 61 and PI were excited at 543 and 633 nm, respectively, and their fluorescence emissions were collected in 640–750 and 650–750 nm, respectively.

**4.3.4. Cell Viability in the Presence of FONs.** Cell viability was evidenced by two methods: time-kill curves and fluorescence spectroscopy using a specific marker.

**4.3.4.1. Time-Kill Curves.** Killing experiments were performed in glass flasks containing Mueller–Hinton (MH) broth with an inoculum of  $1 \times 10^6 \text{ cfu mL}^{-1}$  in the presence of FONs. A flask of inoculated cation adjusted MH broth with no nanoparticles served as control. Surviving bacteria were counted after 0, 3, 6, and 24 h of incubation at  $37^\circ\text{C}$  by subculturing  $50 \mu\text{L}$  of serial dilutions ( $10^{-1}$ ,  $10^{-2}$ , and  $10^{-4}$ ) of samples (in 0.9% NaCl) on MH plates using a spiral plater (Spiral System; Interscience, Saint-Nom-la-Bretèche, France).

**4.3.4.2. Fluorescence Microscopy.** Cell viability was assessed by using PI, a non-permeant red-emitting intercalating agent that stains nucleic acids for bacteria displaying membrane damage. The bacteria, incubated or not with FONs, were treated with a  $30 \mu\text{mol L}^{-1}$  solution of PI for 5 min after 24 h.

**4.4. Fluorescence Microscopy Imaging.** **4.4.1. Confocal Fluorescence Imaging.** Lab-Tek chamber slides were used to image all control, FON, and FON–bacteria samples ( $200 \mu\text{L}$ ). Confocal fluorescence imaging was performed using a Leica TCS SP5 microscope, equipped with an oil-immersion objective (Plan Apo,  $63\times$ ,  $\text{NA} = 1.4$ ) and a monochromator for the emission detection. FON excitation was performed at 488 nm, and the emission signal was collected in the 520–780 nm range in the absence of any other staining agent. Z-stack acquisitions over  $3.5 \mu\text{m}$  with a  $0.5 \mu\text{m}$  z-step were recorded to identify FON localization after bacteria adhesion.

**4.4.2. Wide-Field Imaging.** Epifluorescence imaging was performed using a Nikon Eclipse TI-U inverted microscope equipped with a four-LED illumination source (ScopeLED F; selected LEDs:  $390 \pm 8$  and  $470 \pm 16$  nm), an oil-immersion objective (Plan Apo,  $60\times$ ,  $\text{NA} = 1.4$ ), and a color camera (Nikon, DS-Fi2).

**4.5. Correlative Light Electron Microscopy.** **4.5.1. SEM Imaging.** SEM was performed by using the secondary electron in-lens detector of a JEOL JSM 7600F field-emission scanning electron microscope on samples deposited on ultrasmooth silicon wafers for microcircuit applications purchased from ACM-France or on holey carbon coated copper finder grids to perform cross-correlation with confocal fluorescence imaging.

**4.5.2. Optical Imaging.** Confocal fluorescence imaging was performed using a Nikon A1 microscope, equipped with DPSS lasers as excitation sources (here 488 nm) and an oil-immersion objective (Plan Apo,  $60\times$ ,  $\text{NA} = 1.4$ ). The copper finder grids purchased from Oxford Instruments were placed on a glass coverslip with the holey carbon film toward the microscope objective, and observations were performed on PG samples immobilized on the copper grids rather than on carbon windows that were found to undergo strong heat effects and spatial fluctuations caused by light absorption.

**4.6. Computational Methodology.** DFT and TDDFT calculations were performed on fPOH and fthiaY in THE, which experimentally provides absorption and emission energy spectra close to those for dyes self-assembled as FONs. To gain computation time, the alkoxyphosphonic acid terminal chains for fPOH and fthiaPOH could be replaced with a methyl group because they are not conjugated with the rest of the molecule. Structures were optimized at the PCM-CAM-B3LYP/6-31+G(d) level of theory, and no imaginary frequencies were observed, ensuring that molecules were in their true minimums of the potential energy surfaces. Vertical excitation energies were obtained at the PCM-TD-CAM-B3LYP/6-31+G(d) using the corrected linear response scheme,<sup>57</sup> as such a formalism is optimal for push–pull dyes.<sup>58</sup> All calculations were carried out with the Gaussian16 program,<sup>59</sup> tightening both self-consistent field ( $10^{-10}$  au) and geometry optimization ( $10^{-5}$  au) convergence. Density difference plots shown in the present study were obtained at the PCM-TD-CAM-B3LYP/6-31+G(d) level and are presented with a contour threshold of 0.0008 au. The charge-transfer parameters, namely, the charge-transfer distance  $d_{\text{CT}}$  and the amount of transferred charge  $q_{\text{CT}}$ , have been determined following a Le Bahers procedure.<sup>60,61</sup>

## ■ ASSOCIATED CONTENT

### 📄 Supporting Information

The Supporting Information is available free of charge on the ACS Publications website at DOI: [10.1021/acsomega.8b02603](https://doi.org/10.1021/acsomega.8b02603).

Details on TDDFT computations, complementary confocal fluorescence imaging, SEM imaging of FONs and PG layers (PDF)

## ■ AUTHOR INFORMATION

### Corresponding Author

\*E-mail: [elena.ishow@univ-nantes.fr](mailto:elena.ishow@univ-nantes.fr). Phone: +33-2-5112-5375.

### ORCID

Adèle D. Laurent: [0000-0001-9553-9014](https://orcid.org/0000-0001-9553-9014)

Eléna Ishow: [0000-0002-2965-1224](https://orcid.org/0000-0002-2965-1224)

### Author Contributions

The manuscript was written through contributions of all authors. All authors have given approval to the final version of the manuscript.

### Funding

Région des Pays de la Loire - LUMOMAT RFI program (ONASSIS PhD project).

### Notes

The authors declare no competing financial interest.

## ACKNOWLEDGMENTS

We deeply acknowledge the Région des Pays de la Loire, France, through the LUMOMAT RFI program (ONASSIS PhD project) and the INRA Nantes-Angers Institution for access to electron microscopy facilities. This research used as well French computational resources of the GENCI-CINES/IDRIS (Grants A0020805117) and CCIPL (Centre de Calcul Intensif des Pays de Loire).

## REFERENCES

(1) Pashchenko, O.; Shelby, T.; Banerjee, T.; Santra, S. A Comparison of Optical, Electrochemical, Magnetic, and Colorimetric Point-of-Care Biosensors for Infectious Disease Diagnosis. *ACS Infect. Dis.* **2018**, *4*, 1162–1178.

(2) Chin, C. D.; Chin, S. Y.; Laksanapopin, T.; Sia, S. K., Low-Cost Microdevices for Point-of-Care Testing. In *Point-of-Care Diagnostics on a Chip*; Iassadore, D.; Westerwelt, R. M., Eds; Springer-Verlag: Berlin, Germany, 2013; p 226.

(3) Holzinger, M.; Le Goff, A.; Cosnier, S. Nanomaterials for Biosensing Applications: A Review. *Front. Chem.* **2014**, *2*, 63.

(4) Kuss, S.; Amin, H. M. A.; Compton, R. G. Electrochemical Detection of Pathogenic Bacteria-Recent Strategies, Advances and Challenges. *Chem. Asian J.* **2018**, *13*, 2758–2769.

(5) Liong, M.; Hoang, A. N.; Chung, J.; Gural, N.; Ford, C. B.; Min, C.; Shah, R. R.; Ahmad, R.; Fernandez-Suarez, M.; Fortune, S. M.; Toner, M.; Lee, H.; Weissleder, R. Magnetic Barcode Assay for Genetic Detection of Pathogens. *Nature Commun.* **2013**, *4*, 1752.

(6) Lee, J. J.; Jeong, K. J.; Hashimoto, M.; Kwon, A. H.; Rwei, A.; Shankarappa, S. A.; Tsui, J. H.; Kohane, D. S Synthetic Ligand-Coated Magnetic Nanoparticles for Microfluidic Bacterial Separation from Blood. *Nano Lett.* **2014**, *14*, 1–5.

(7) Pramanik, A.; Jones, S.; Pedraza, F.; Vangara, A.; Sweet, C.; Williams, M. S.; Rупpa-Kasani, V.; Risher, S. E.; Sardar, D.; Ray, P. C. Fluorescent, Magnetic Multifunctional Carbon Dots for Selective Separation, Identification, and Eradication of Drug-Resistant Superbugs. *ACS Omega* **2017**, *2*, 554–562.

(8) Boudjemaa, R.; Briandet, R.; Fontaine-Aupart, M. P.; Steenkeste, K. How Do Fluorescence Spectroscopy and Multimodal Fluorescence Imaging Help to Dissect the Enhanced Efficiency of the Vancomycin-Rifampin Combination against *Staphylococcus aureus* Infections? *Photochem. Photobiol. Sci.* **2017**, *16*, 1391–1399.

(9) Tokel, O.; Inci, F.; Demirci, U. Advances in Plasmonic Technologies for Point of Care Applications. *Chem. Rev.* **2014**, *114*, 5728–5752.

(10) Yuan, P.; Ding, X.; Yang, Y. Y.; Xu, Q. H. Metal Nanoparticles for Diagnosis and Therapy of Bacterial Infection. *Adv. Healthcare Mater.* **2018**, *7*, 1701392.

(11) Galvan, D. D.; Yu, Q. Surface-Enhanced Raman Scattering for Rapid Detection and Characterization of Antibiotic-Resistant Bacteria. *Adv. Healthcare Mater.* **2018**, *7*, 1701335.

(12) Saha, K.; Agasti, S. S.; Kim, C.; Li, X.; Rotello, V. M. Gold Nanoparticles in Chemical and Biological Sensing. *Chem. Rev.* **2012**, *112*, 2739–2779.

(13) Valeur, B.; Berberan-Santos, M. N., *Molecular Fluorescence: Principles and Applications*, 2nd ed.; Wiley VCH Verlag: Weinheim, Germany, 2012; p 592.

(14) Shi, J.; Chan, C.; Pang, Y.; Ye, W.; Tian, F.; Lyu, J.; Zhang, Y.; Yang, M. A Fluorescence Resonance Energy Transfer (FRET) Biosensor Based on Graphene Quantum Dots (GQDs) and Gold Nanoparticles (AuNPs) for the Detection of *mecA* Gene Sequence of *Staphylococcus aureus*. *Biosens. Bioelectron.* **2015**, *67*, 595–600.

(15) Takemura, K.; Adegoke, O.; Takahashi, N.; Kato, T.; Li, T. C.; Kitamoto, N.; Tanaka, T.; Suzuki, T.; Park, E. Y. Versatility of A Localized Surface Plasmon Resonance-Based Gold Nanoparticle-Alloyed Quantum Dot Nanobiosensor for Immunofluorescence Detection of Viruses. *Biosens. Bioelectron.* **2017**, *89*, 998–1005.

(16) Disney, M. D.; Zheng, J.; Swager, T. M.; Seeberger, P. H. Detection of Bacteria with Carbohydrate-Functionalized Fluorescent Polymers. *J. Am. Chem. Soc.* **2004**, *126*, 13343–13346.

(17) Yuan, H.; Liu, Z.; Liu, L.; Lv, F.; Wang, Y.; Wang, S. Cationic Conjugated Polymers for Discrimination of Microbial Pathogens. *Adv. Mater.* **2014**, *26*, 4333–4338.

(18) Gao, T.; Zeng, H.; Xu, H.; Gao, F.; Li, W.; Zhang, S.; Liu, Y.; Luo, G.; Li, M.; Jiang, D.; Chen, Z.; Wu, Y.; Wang, W.; Zeng, W. Novel Self-assembled Organic Nanoprobe for Molecular Imaging and Treatment of Gram-Positive Bacterial Infection. *Theranostics* **2018**, *8*, 1911–1922.

(19) Zhao, E.; Chen, Y.; Chen, S.; Deng, H.; Gui, C.; Leung, C. W. T.; Hong, Y.; Lam, J. W. Y.; Tang, B. Z. A Luminogen with Aggregation-Induced Emission Characteristics for Wash-Free Bacterial Imaging, High-Throughput Antibiotics Screening and Bacterial Susceptibility Evaluation. *Adv. Mater.* **2015**, *27*, 4931–4937.

(20) Sohlenkamp, C.; Geiger, O. Bacterial Membrane Lipids: Diversity in Structures and Pathways. *FEMS Microbiol. Rev.* **2016**, *40*, 133–159.

(21) Vollmer, W.; Blanot, D.; De Pedro, M. A. Peptidoglycan Structure and Architecture. *FEMS Microbiol. Rev.* **2008**, *32*, 149–167.

(22) Turner, R. D.; Vollmer, W.; Foster, S. J. Different Walls for Rods and Balls: The Diversity of Peptidoglycan. *Mol. Microbiol.* **2014**, *91*, 862–874.

(23) Romaniuk, J. A. H.; Cegelski, L. Peptidoglycan and Teichoic Acid Levels and Alterations in *Staphylococcus aureus* by Cell-Wall and Whole-Cell Nuclear Magnetic Resonance. *Biochemistry* **2018**, *57*, 3966–3975.

(24) Reynolds, M.; Marradi, M.; Imberty, A.; Penades, S.; Perez, S. Multivalent Gold Glycoclusters: High Affinity Molecular Recognition by Bacterial Lectin PA-IL. *Chem. Eur. J.* **2012**, *18*, 4264–4273.

(25) Beausart, A.; Beloin, C.; Ghigo, J. M.; Chapot-Chartier, M. P.; Kulakauskas, S.; Duval, J. F. L. Probing The Influence of Cell Surface Polysaccharides on Nanodendrimer Binding to Gram-Negative and Gram-Positive Bacteria Using Single-Nanoparticle Force Spectroscopy. *Nanoscale* **2018**, *10*, 12743–12753.

(26) Feng, Z. V.; Gunsolus, I. L.; Qiu, T. A.; Hurley, K. R.; Nyberg, L. H.; Frew, H.; Johnson, K. P.; Vartanian, A. M.; Jacob, L. M.; Lohse, S. E.; Torelli, M. D.; Hamers, R. J.; Murphy, C. J.; Haynes, C. L. Impacts of Gold Nanoparticle Charge and Ligand Type on Surface Binding and Toxicity to Gram-Negative and Gram-Positive Bacteria. *Chem. Sci.* **2015**, *6*, 5186–5196.

(27) Zhao, Y.; Tian, Y.; Cui, Y.; Liu, W.; Ma, W.; Jiang, X. Small Molecule-Capped Gold Nanoparticles as Potent Antibacterial Agents That Target Gram-Negative Bacteria. *J. Am. Chem. Soc.* **2010**, *132*, 12349–12356.

(28) Richards, S.-J.; Isufi, K.; Wilkins, L. E.; Lipecki, J.; Fullam, E.; Gibson, M. I. Multivalent Antimicrobial Polymer Nanoparticles Target Mycobacteria and Gram-Negative Bacteria by Distinct Mechanisms. *Biomacromolecules* **2018**, *19*, 256–264.

(29) Mazrad, Z. A. I.; Choi, C. A.; Kwon, Y. M.; In, I.; Lee, K. D.; Park, S. Y. Design of Surface-Coatable NIR-Responsive Fluorescent Nanoparticles with PEI Passivation for Bacterial Detection and Killing. *ACS Appl. Mater. Interfaces* **2017**, *9*, 33317–33326.

(30) Lyden, A.; Lombardi, L.; Sire, W.; Li, P.; Simpson, J. C.; Butler, G.; Lee, G. U. Characterization of Carboxylate Nanoparticle Adhesion with The Fungal Pathogen *Candida albicans*. *Nanoscale* **2017**, *9*, 15911–15922.

(31) Pillai, P. P.; Kowalczyk, B.; Kandere-Grzybowska, K.; Borkowska, M.; Grzybowski, B. A. Engineering Gram Selectivity of Mixed-Charge Gold Nanoparticles by Tuning the Balance of Surface Charges. *Angew. Chem., Int. Ed.* **2016**, *55*, 8610–8614.

(32) Kyuji, O. Prediction of pKa Values of Akylphosphonic Acids. *Bull. Chem. Soc. Jpn.* **1992**, *65*, 2543–2545.

(33) Franz, R. G. Comparisons of pKa and Log P Values of Some Carboxylic and Phosphonic Acids: Synthesis and Measurement. *AAPS PharmSci* **2001**, *3*, 1–13.

- (34) Tan, J.; Gemeinhart, R. A.; Ma, M.; Saltzman, W. M. Improved Cell Adhesion and Proliferation on Synthetic Phosphonic Acid-Containing Hydrogels. *Biomaterials* **2005**, *26*, 3663–3671.
- (35) Telegdi, J.; Rigó, T.; Beczner, J.; Kálmán, E. Influence of Langmuir–Blodgett Nanolayers on Microbial Adhesion. *Surf. Eng.* **2005**, *21*, 107–112.
- (36) Metcalf, W. W.; van der Donk, W. A. Biosynthesis of Phosphonic and Phosphinic Acid Natural Products. *Annu. Rev. Biochem.* **2009**, *78*, 65–94.
- (37) Sevrain, C. M.; Berchel, M.; Couthon, H.; Jaffrès, P.-A. Phosphonic Acid: Preparation and Applications. *Beilstein J. Org. Chem.* **2017**, *13*, 2186–2213.
- (38) Falagas, M. E.; Vouloumanou, E. K.; Samonis, G.; Vardakas, K. Z. Fosfomycin. *Clin. Microbiol. Rev.* **2016**, *29*, 321–347.
- (39) Hendlin, D.; Stapley, E. O.; Jackson, M.; Wallick, H.; Miller, A. K.; Wolf, F. J.; Miller, T. W.; Chaiet, L.; Kahan, F. M.; Foltz, E. L.; Woodruff, H. B.; Mata, J. M.; Hernandez, S.; Mochales, S. Phosphonomycin, a New Antibiotic Produced by Strains of *Streptomyces*. *Science* **1969**, *166*, 122–123.
- (40) Fischer, I.; Petkau-Milroy, K.; Dorland, Y. L.; Schenning, A. P. H.; Brunsveld, L. Self-Assembled Fluorescent Organic Nanoparticles for Live-Cell Imaging. *Chem. Eur. J.* **2013**, *19*, 16646–16650.
- (41) Reddy, E. R.; Yellanki, S.; Medishetty, R.; Konada, L.; Alamuru, N. P.; Haldar, D.; Parsa, K. V. L.; Kulkarni, P.; Rajadurai, M. Red Fluorescent Organic Nanoparticle Bioprobes: A Photostable Cytoplasmic Stain for Long Term in Vitro and in Vivo Visualization. *ChemNanoMat* **2015**, *1*, 567–576.
- (42) Boucard, J.; Linot, C.; Blondy, T.; Nedellec, S.; Hulin, P.; Blanquart, C.; Lartigue, L.; Ishow, E. Small Molecule-Based Fluorescent Organic Nanoassemblies with Strong Hydrogen Bonding Networks for Fine Tuning and Monitoring Drug Delivery in Cancer Cells. *Small* **2018**, *14*, 1802307.
- (43) Radkov, A. D.; Hsu, Y. P.; Booher, G.; VanNieuwenhze, M. S. Imaging Bacterial Cell Wall Biosynthesis. *Annu. Rev. Biochem.* **2018**, *87*, 991–1014.
- (44) Faucon, A.; Maldiney, T.; Clément, O.; Hulin, P.; Nedellec, S.; Robard, M.; Gautier, N.; De Meulenaere, E.; Clays, K.; Orlando, T.; Lascialfari, A.; Fiorini-Debuisschert, C.; Fresnais, J.; Ishow, E. Highly Cohesive Dual Nanoassemblies for Complementary Multiscale Bioimaging. *J. Mater. Chem. B* **2014**, *2*, 7747–7755.
- (45) Faucon, A.; Lenk, R.; Hemez, J.; Gautron, E.; Jacquemin, D.; Le Questel, J.-Y.; Graton, J.; Brosseau, A.; Ishow, E. Fluorescent Carboxylic and Phosphonic Acids: Comparative Photophysics from Solution to Organic Nanoparticles. *Phys. Chem. Chem. Phys.* **2013**, *15*, 12748–12756.
- (46) Breton, M.; Prevel, G.; Audibert, J. F.; Pansu, R.; Tauc, P.; Le Pioufle, B.; Francais, O.; Fresnais, J.; Berret, J. F.; Ishow, E. Solvatochromic Dissociation of Non-Covalent Fluorescent Organic Nanoparticles upon Cell Internalization. *Phys. Chem. Chem. Phys.* **2011**, *13*, 13268–13276.
- (47) Daniel, J.; Bondu, F.; Adamietz, F.; Blanchard-Desce, M.; Rodriguez, V. Interfacial Organization in Dipolar Dyes-based Organic Nanoparticles probed by Second-Harmonic Scattering. *ACS Photonics* **2015**, *2*, 1209–1216.
- (48) Ishow, E.; Guillot, R.; Buntinx, G.; Poizat, O. Photoinduced Intramolecular Charge-Transfer Dynamics of A Red-Emitting Dicyanovinyl-Based Triarylamine Dye in Solution. *J. Photochem. Photobiol. A: Chem.* **2012**, *234*, 27–36.
- (49) Tuson, H. H.; Auer, G. K.; Renner, L. D.; Hasebe, M.; Tropini, C.; Salick, M.; Crone, W. C.; Gopinathan, A.; Huang, K. C.; Weibel, D. B. Measuring the Stiffness of Bacterial Cells from Growth Rates in Hydrogels of Tunable Elasticity. *Mol. Microbiol.* **2012**, *84*, 874–891.
- (50) Kuznetsova, T. G.; Starodubtseva, M. N.; Yegorenkov, N. I.; Chizhik, S. A.; Zhdanov, R. I. Atomic force microscopy probing of cell elasticity. *Micron* **2007**, *38*, 824–833.
- (51) Chung, H. J.; Reiner, T.; Budin, G.; Min, C.; Liong, M.; Issadore, D.; Lee, H.; Weissleder, R. Ubiquitous Detection of Gram-Positive Bacteria with Bioorthogonal Magnetofluorescent Nanoparticles. *ACS Nano* **2011**, *5*, 8834–8841.
- (52) Kell, A. J.; Stewart, G.; Ryan, S.; Peytavi, R.; Boissinot, M.; Huletsky, A.; Bergeron, M. G.; Simard, B. Vancomycin-Modified Nanoparticles for Efficient Targeting and Preconcentration of Gram-Positive and Gram-Negative Bacteria. *ACS Nano* **2008**, *2*, 1777–1788.
- (53) Faucon, A.; Benhelli-Mokrani, H.; Córdova, L. A.; Brulin, B.; Heymann, D.; Hulin, P.; Nedellec, S.; Ishow, E. Are Fluorescent Organic Nanoparticles Relevant Tools for Tracking Cancer Cells or Macrophages. *Adv. Healthcare Mater.* **2015**, *4*, 2727–2734.
- (54) Hartmann, M.; Berditsch, M.; Hawecker, J.; Ardakani, M. F.; Gerthsen, D.; Ulrich, A. S. Damage of the Bacterial Cell Envelope by Antimicrobial Peptides Gramicidin S and PGLa as Revealed by Transmission and Scanning Electron Microscopy. *Antimicrob. Agents Chemother.* **2010**, *54*, 3132–3142.
- (55) Hayden, S. C.; Zhao, G.; Saha, K.; Phillips, R. L.; Li, X.; Miranda, O. R.; Rotello, V. M.; El-Sayed, M. A.; Schmidt-Krey, I.; Bunz, U. H. F. Aggregation and Interaction of Cationic Nanoparticles on Bacterial Surfaces. *J. Am. Chem. Soc.* **2012**, *134*, 6920–6923.
- (56) Millenbaugh, N.; Baskin, J.; DeSilva, M.; Elliott, W. R.; Glickman, R. Photothermal Killing of *Staphylococcus aureus* Using Antibody-Targeted Gold Nanoparticles. *Int. J. Nanomed.* **2015**, *10*, 1953–1960.
- (57) Caricato, M.; Mennucci, B.; Tomasi, J.; Ingrosso, F.; Cammi, R.; Corni, S.; Scalmani, G. Formation and Relaxation of Excited States in Solution: A New Time Dependent Polarizable Continuum Model Based on Time Dependent Density Functional Theory. *J. Chem. Phys.* **2006**, *124*, 124520.
- (58) Laurent, A. D.; Jacquemin, D. TD-DFT Benchmarks: A Review. *Int. J. Quantum Chem.* **2013**, *113*, 2019–2039.
- (59) Frisch, M. J.; Trucks, G. W.; Schlegel, H. B.; Scuseria, G. E.; Robb, M. A.; Cheeseman, J. R.; Scalmani, G.; Barone, V.; Petersson, G. A.; Nakatsuji, H.; et al. *Gaussian 16*, Revision 01; Gaussian, Inc.: Wallingford, CT, 2016.
- (60) Jacquemin, D.; Le Bahers, T.; Adamo, C.; Ciofini, I. What Is The “Best” Atomic Charge Model to Describe Through-Space Charge-Transfer Excitations? *Phys. Chem. Chem. Phys.* **2012**, *14*, 5383–5388.
- (61) Le Bahers, T.; Adamo, C.; Ciofini, I. A Qualitative Index of Spatial Extent in Charge-Transfer Excitations. *J. Chem. Theory Comput.* **2011**, *7*, 2498–2506.